

Computational Methods for Electrical Impedance Tomography

Jose Alanis^{1,a}, Soledad Farber^{2,a}, Shelby Horth^{3,a}, Nicholas Wharff^{4,a},
Mason Manning⁵, and
Mentor: Malena Español⁵

¹Sacramento State University, Sacramento CA, United States

²Freed-Hardeman University, Henderson TN, United States

³Wake Forest University, Winston-Salem NC, United States

⁴Drake University, Des Moines IA, United States

⁵Arizona State University, Tempe AZ, United States

^aSimon A. Levin Mathematical, Computational, and Modeling Sciences
Center: Quantitative Research for the Life & Social Sciences Program,
Arizona State University, Tempe AZ, United States

July 2022

Abstract

Electrical Impedance Tomography (EIT) is a low-cost, portable, and noninvasive imaging system that does not use ionizing radiation. Though it has seen promising use in many applications including the continuous monitoring of the lungs and detection of cancerous regions in the body, it has potential for industrial uses beyond what is typically recognized in human medicine. However, EIT formulates a very challenging, nonlinear, highly ill-posed problem. Over the past few decades, many approaches have been introduced by incorporating the advancements in traditional methods. However, those approaches lack clinical and experimental versatility as there is still disagreement over which proposed algorithms are most successful. Therefore, we investigate, develop, and implement new regularization methods using deep neural network (DNN) approaches for solving the EIT inverse problem. In this study, we explore the use of first, second, and third order derivative regularization operators, Krylov methods, and distinct neural network architectures. We compare our approaches with traditional EIT methods and present the results of each technique with respect to improvement (or loss) in spatial resolution as well as influence on computational cost.

1 Introduction

One of the main imaging modalities that has seen a significant increase in recent years is the noninvasive, nonionizing, and radiation-free imaging technique of Electrical Impedance Tomography (EIT) [5]. EIT is a process used to create tomographic images of the electrical properties of the tissues within a subject based on electrical impulse measurements from body surface electrodes [1]. While there are a wide variety of applications for this technique, EIT is seeing its most widespread usage in the monitoring of pulmonary ventilation of intensive care and surgical patients [2]. In addition, EIT is showing promise for applications in many other areas of science and engineering, including geophysics and biology [23, 42]. Nevertheless, despite the advantages of producing high-contrast images and acquiring data through harmless electrical impedance measurements, the image recovery process of characterizing the EIT image from the current and voltage measurement data is a severely ill-posed nonlinear inverse problem which requires a noise-robust regularization strategy for precise reconstruction of an otherwise poor-quality solution [13]. The voltage data is usually highly corrupted with unknown levels of Gaussian noise, and consequently, the recovered solutions are highly sensitive to small perturbations in the observations, rendering the inverse problem difficult to solve.

One limitation of solving the EIT problem is that most clinical and physiological research for medical imaging is being done using older and proprietary imaging algorithms. Reconstructed images from these more traditional methods show non-uniformity in factors including amplitude response, position error, spatial resolution, shape deformation, ringing, and noise amplification [1]. In response, many other approaches to the EIT inverse problem have been introduced, incorporating advances that have been made over the past few decades. However, they lack clinical and experimental versatility as there is still disagreement about which proposed methods are best or how they can be combined for optimal output [1].

To address this issue, we explore a variety of regularization methods and compare them against each other. Additionally, we compare these to Deep Neural Network (DNN) approaches to reach a feasible consensus on the improved efficacy in the characterization of the reconstructed images and collate numerical validity of each method’s impact on spatial resolution given its computational cost.

Reconstructions of EIT typically use regularization techniques, such as Tikhonov Regularization [22], Krylov Methods [12], and Total Variation (TV) Regularization [18] in our case, that yield an approximation of the respective solution function. Typically, these methods require careful consideration of boundary conditions, but these are set by the EIT problem. Such conditions can be overcome, but they are computationally demanding, as modeled in the use of a Krylov method [5]. Iterative methods used for approximating solutions for nonlinear problems easily fall into local solutions due to their linear nature which causes a large amount of loss during image reconstruction [18]. Therefore, unless we linearize the problem, as we’ll see using more traditional methods, iterative methods are relatively sensitive to disturbances in the data, causing the reconstructed images to suffer from a lack of sharpness or clarity. These imbalances must be corrected with sophisticated modeling techniques. Thus, it is challenging to account for the uncertainties in the data set including unknown electrode locations, boundary shape, or contact impedances [9, 17, 26].

The spectrum of non-iterative EIT imaging solutions comprises of methods including Linear Back Propagation [35], the Sensitivity Coefficient [25], and Truncated Singular

Value Decomposition [39]. However, for under-sampled imaging, direct image reconstruction contains severe artifacts that iterative methods lack. This is because iterative methods typically optimize an objective function containing spatial or temporal constraints [40]. Therefore, we aim to exercise recent advances in the larger scale field of image reconstruction by exploring the influence of Deep Learning and Neural Networks for faster, more direct iterative procedures.

In this study, with the help of physical modeling, we simulate capable reconstruction algorithms that produce EIT images by utilizing iterative and non-iterative algorithms as well as deep neural networks and compare the resolution and computational efficiency of each technique against one another. We show that while iterative techniques improve the insensitivity to noise given incomplete data, Deep Neural Networks (DNN) are not only well suited for the post-processing of initial data but also for the preserving of two-dimensional structure information [18]. By obtaining local features of the unknown solution through filters (hidden layers) and training the DNN to remove destructive artifacts, the received content of the reconstructed image is improved. More specifically, this paper explores approaches that use EIT simulated data to train and develop an efficient DNN model. Following training, it can then be adjusted to cope with the untrained experimental data, and compare the produced imaging results of the experimental measurements' data to more traditional methods.

2 Methods

2.1 Model Description and Derivative Operators

Electrical impedance tomography is a nonlinear inverse problem in which we aim to calculate the conductivities of the volume inside of a subject from the observed current to voltage measurements at boundary electrodes. We start by considering the linear model

$$Ax = b = b_{\text{true}} + e \quad (1)$$

where A is the model matrix with dimension $m \times n$, b is the vector of voltage differences, b_{true} is the unknown vector of true values, e is the unknown vector of observation errors, and x is the unknown list of parameters that characterize the reconstructed image in vectorized form [29]. Then, for any given vector x , we can calculate a residual vector $r(x) = Ax - b$, our goal being to find the x that produces a residual vector with the least magnitude.

We find the solution x by obtaining estimates of the solution vector \hat{x} and the norm of the residual vector using minimization functions such as

$$\min_x \{ \|Ax - b\|_2^2 \}.$$

This generates a solution that fits the system according to the Euclidean (L_2) norm [29]. However, we then examine

$$\min_x \{ \|Ax - b\|_2^2 + \lambda \|x\|_2^2 \}$$

which incorporates a regularization term to reduce the noise influence of the estimated parameters. However, it is important to note that when the regularization parameter is

too high, there is an increased prevalence of inconsistencies in the output. To account for this flaw, we explore the addition of a derivative operator which can be modeled with the General Tikhonov Regularization equation

$$\min_x \{ \|Ax - b\|_2^2 + \lambda \|Lx\|_2^2 \}, \quad (2)$$

where L is an $n \times n$ matrix chosen according to the factor of an image that is looking to be optimized [27]. For instance, edge detection is one of the most frequently utilized techniques in digital image processing. As first order derivative operators are based on approximations of the 2-D gradient across an image, such operators work well at calculating the gradient of image intensity at each pixel, indicating the largest increase from light to dark as well as the direction [36]. However, second order derivative operators have the zero crossing property and are therefore more efficiently utilized for detecting regions of the image with rapid intensity changes, otherwise known as edges [4]. The difference in application between first and second derivative operators is modeled in Figure 3.

First order derivative operators are useful in minimizing the objective function (2) by identifying smoother derivations in brightness while suffering from problems such as staircase artifacts and loss in smooth intensity changes for textures and low-contrast objects [16]. To compare the advantages and limitations of first and second order derivative operators, we approximate the gradient using first order derivative operators [31]:

$$f'(x) \cong \frac{f(x+h) - f(x)}{h} \quad (3)$$

$$f'(x) \cong \frac{f(x) - f(x-h)}{h} \quad (4)$$

$$f'(x) \cong \frac{f(x+h) - f(x-h)}{2h} \quad (5)$$

$$\frac{1}{h} \begin{bmatrix} -1 & 1 & 0 & \dots \\ 0 & -1 & 1 & \dots \\ \vdots & & \ddots & 1 \\ 0 & \dots & \dots & -1 \end{bmatrix} \begin{bmatrix} f(x_1) \\ f(x_2) \\ \vdots \\ f(x_n) \end{bmatrix}$$

Figure 1: Example of a matrix L as a first derivative operator approximating equation (3) for a one-dimensional system. h is the chosen interval size and $f(x_i)$ is the corresponding dependent approximation at $x_i = x + (i-1)h$ starting at $i = 1$ [31]

Then we observe the effects of the second order derivative operators:

$$f''(x) \cong \frac{f(x+h) - 2f(x) + f(x-h)}{2h} \quad (6)$$

$$\underbrace{\begin{bmatrix} 0 & -1 & -1 \\ -1 & 4 & -1 \\ -1 & -1 & 0 \end{bmatrix}}_{\text{Negative Laplacian Operator}}, \quad \underbrace{\begin{bmatrix} 0 & 1 & 1 \\ 1 & -4 & 1 \\ 1 & 1 & 0 \end{bmatrix}}_{\text{Positive Laplacian Operator}} \quad (7)$$

The purpose of exploring the Laplacian operator is to determine how alternative operators affect the efficacy of edge localization of a given image reconstruction function. While (6) approximates the second derivative with respect to abrupt changes in brightness intensity, the Laplacian operators (7) take out edges in a particular direction depending on whether the positive or negative operator is imposed [37]. Particularly, the Laplacian operators work to highlight gray level discontinuities and deemphasize regions with slowly varying gray levels.



(a) Result of applying the negative Laplacian operator to an image [10]. (b) Result of applying the positive Laplacian operator to an image [10].

Figure 2: The negative Laplacian operator takes out inward edges and displays them against a dark background (a) while the positive Laplacian operator takes out outward edges and displays them against the same dark background (b) [15] [37]. Therefore, one must either subtract the positive Laplacian operator resultant from the original image or add the negative Laplacian operator resultant to the original image for sharper resolution. However, it is important to note that the Laplacian operator is not used for one-dimensional systems. If used, it generates a scalar field with broad discrepancies between itself and the objective function as shown in Figure [11].

In addition to first and second order derivative operators, we assess the influence of third derivative operators (8) and integral operators (9):

$$f'''(x) \cong \frac{f(x+2h) - 2f(x+h) + 2f(x-h) - f(x-2h)}{2h^3} \quad (8)$$

$$\int_a^b f(x) dx \cong \frac{b-a}{2} \times [f(b) - f(a)] \quad (9)$$

Third derivative operators such as (8) are constructed through a process similar to deriving operators (3), (4), and (5). They cooperate in giving more accurate localization of edges (6). However, higher derivatives are more sensitive to noise, as can be seen in the comparison of solving the minimization problem, using various derivative operators, posed in Figures (8, 9, 10, 11) and 12.

As we are dealing with discrete models as practical models for image restoration, integral operators (9) produce piecewise constant approximations of the objective model by assuming continuity (21). This suppresses the model error caused by the discrete models, allowing for the localization of edges, as well as distinction between differentiable and non-differentiable intervals. As we observe in Figures (8, 9) and (10), first, second, and third order derivative operators improve edge detection respectively. However, estimation of the solution function on more differentiable intervals becomes less accurate. Integral operators work well for locally approximating the solution function to account for these differences in the minimization function's behavior (24).

Now, after incorporating the regularization term into the minimization function, we look at the implementation of other norms, as opposed to utilizing the L_2 norm as a default, in defining a measurement of magnitude of the least error between the objective and various proposed minimization functions.

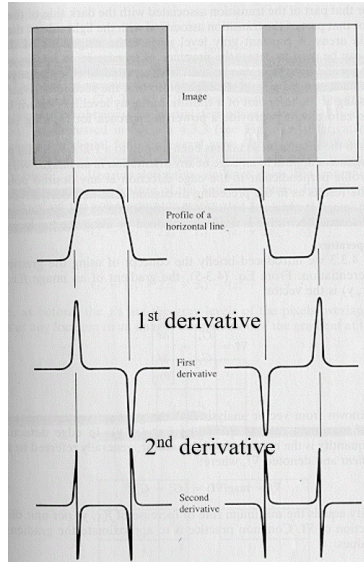


Figure 3: An example of how first and second order derivative operators work in edge detection. (7).

2.2 Norms, Iteratively Reweighted Least Squares & Total Variation

We further experimented with one-dimensional image reconstruction by examining iteratively reweighted norm algorithms for total variation regularization. Iteratively Reweighted Least Squares (IRLS) is used for denoising and deconvolution, so it generally improves resolution and contrast for digital images. The algorithm typically utilizes the Manhattan distance (L_1 norm) or the Euclidean norm. For instance, (2) can be modified into

$$\min_x \left\{ \|Ax - b\|_2^2 + \lambda \|Lx\|_1 \right\},$$

where the L_1 norm of the regularization term is taken because it is more robust than the L_2 norm, computing the cost of outliers linearly as opposed to exponentially [33]. However, from a theoretical perspective, there are many other ways of constructing the optimization function, with no definite systematic comparison between them because of competing performance measures of various imaging modalities [32].

Branching off of the concept of IRLS, Total Variation (TV) essentially allows for more flexibility within the algorithm. A sample TV method utilizes the equation:

$$\min_x \left\{ \frac{1}{p} \|Ax - b\|_p^p + \frac{\lambda}{q} \|Lx\|_q \right\}, \quad (10)$$

where p and q represent respective norms looking to be implemented. Methods that exercise this TV aspect can apply a wide variety of norms to regularized inversions with the intention of improving the data fidelity and regularization terms [38]. It is important to consider the cost of using such equations in an iterative process. Since there is no real time variable, and the only connection that exists is between two approximations at each iteration, an observed problem is that it is difficult to find the trajectory of these errors over time. With an open boundary like this, performing fewer or more iterations than necessary will yield a less precise solution [33]. Hence, boundary conditions should be imposed.

A modified TV functional that has attracted attention is the equation

$$\min_x \left\{ \frac{1}{p} \|Ax - b\|_p^p + \frac{\lambda}{q} \left\| \sqrt{(D_x x)^2 + (D_y x)^2} \right\|_q^q \right\},$$

where $\left\| \sqrt{(D_x x)^2 + (D_y x)^2} \right\|$ is the total variation of x , and D_x, D_y denote the horizontal and vertical discrete derivative operators respectively in a two-dimensional system. It is important to note that in a one-dimensional system, we exclude the $(D_y x)^2$ term [33]. Now, the solution is approximated within an iterative scheme by incorporating a regularized weighted matrix W_R as well as a functional weighted matrix W_F in the solution estimate, both of which are recalculated based on the previous x estimation. This seeks a way to implement the manipulation of the observed data points and weight their influence on the solution approximation.

At each iteration k , define

$$x^{(0)} = (A^T A + \lambda D^T D)^{-1} A^T b$$

$$W_F^{(k)} = \text{diag} \left(\frac{2}{p} \mathfrak{f}_F (Ax^{k-1} - b) \right)$$

$$W_R^{(k)} = \text{diag} \left(\frac{2}{q} \mathfrak{f}_R \left((D_x x^{k-1})^2 + (D_y x^{k-1})^2 \right) \right)$$

$$x^k = (A^T W_F^k A + \lambda D_x^T W_R^k D_x + \lambda D_y^T W_R^k D_y)^{-1} A^T W_F^k b,$$

where $x^{(0)}$ is the initial solution approximation, and x^k is the updated solution approximation at iteration k [33]. Additionally,

$$\mathfrak{f}_F(x) = \begin{cases} |x|^{p-2} & , \text{ if } |x| > \epsilon_F \\ \epsilon_F^{p-2} & , \text{ if } |x| \leq \epsilon_F \end{cases}$$

$$\mathfrak{f}_R(x) = \begin{cases} |x|^{\frac{q-2}{2}} & , \text{ if } |x| > \epsilon_R \\ 0 & , \text{ if } |x| \leq \epsilon_R \end{cases}.$$

The motivation for setting \mathfrak{f}_R below the threshold value is that a region with very small or zero gradient should have an insignificant contribution to the regularization term. These functions play an active role in the reweighting process because not only are they applied to matrices W_R and W_F , but they also get updated depending on a very small threshold value.

The epsilon value is determined according to the piecewise function equations depending on if all of the values in the W matrices are above or below the threshold value [8].

This iterative process is also commonly referred to as robust regression. It is a way of mitigating the influence of outliers in an otherwise normally-distributed data set. Robust regression is commonly used when the number of variables in a linear system exceeds the number of observations [19]. In EIT there is only one observation: noisy vector b . However, there are two variables: x and noise. Hence, we use this process to assign a weight to each data point. This method is less sensitive to perturbations in the data and therefore less sensitive to outliers than standard least squares.

Iteratively changing these weights provides an additional factor which improves the fit. To compute weights, we use the predefined weight function. The algorithm then computes new model coefficients and iteration terminates when the values of the coefficient estimates converge within a specified tolerance [33]. However, this still poses the same boundary error as [10].

2.3 Larger Scale Problems

After modeling the EIT inverse problem using the standard matrix-vector equation (1), we move to a more sophisticated representation of our system. The problem can be modeled using the equation:

$$\nabla \cdot (\sigma \nabla u) = 0.$$

This is a mathematical model for the propagation of electromagnetic fields in the body as derived from Maxwell's equations [27]. This measures the electrical potential u inside of a given domain for a given conductivity σ and boundary condition.

At the electrical impulse frequencies used in EIT, voltages distribute according to $\nabla \cdot (\sigma \nabla u) = 0$ with imposed boundary conditions. This is to say that EIT is non-local. Thus every change in conductivity affects the voltage measurements throughout the remainder of the region, leading to the ill-conditioning of the image reconstruction.

We can then transform (1) into

$$S \Delta \sigma = \Delta v \quad (11)$$

where S is the sensitivity matrix as denoted in Figure 4 [2]. In order to reconstruct an image, sensitivity explains what each measurement means and which regions of the subject could be generating the measurements observed. Δv represents the voltages measured at the receiving electrode after the electrical signal has passed through the subject and experienced resistance due to varying conductivities. $\Delta \sigma$ is what we want to determine because it consists of conductivity measurements, in a vectorized form, and how they vary throughout the region of interest. This gives us information about what the image should look like and how to construct it.

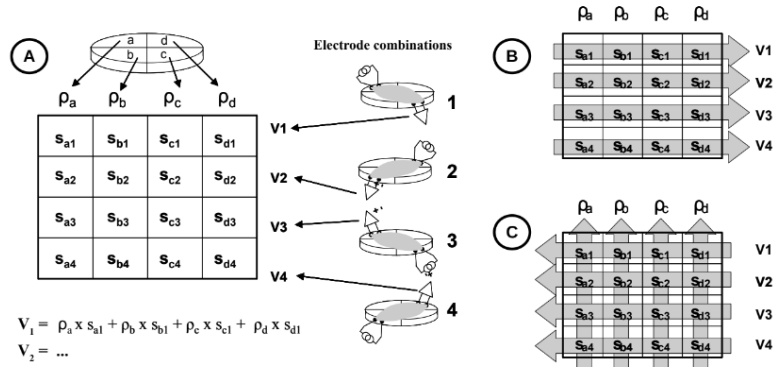


Figure 4: For simplicity, this model uses four electrodes and divides the subject's region into four voxels. The sensitivity matrix is constructed so that each column represents the resistivity of each voxel and each row represents the voltage of each receiving electrode. Each entry in the sensitivity matrix denotes a weight that indicates the extent to which the corresponding voxel affects the overall voltage. Thus, each voltage can be calculated as a matrix decomposition of the sum of resistivity in each voxel weighted by a factor S [2].

Adapting to a larger scale problem, we use the sensitivity matrix to explore the leverage of image reconstruction techniques such as the Truncated Singular Value Decomposition (TSVD) and the Generalized Krylov Subspace algorithmic framework.

The Singular Value Decomposition is used for inverse problems for which there are no analytical solutions, as is the case in EIT [20]. The advantage of using the non-iterative TSVD approach is that it is used for quick and accurate image reconstruction. TSVD is a multi-resolution strategy that reduces the size of the system as a way to reserve memory capacity given the large scope of this problem [41]. However, spatial resolution is compromised due to the non-iterative nature of the process. This is because smaller singular values magnify projection noise. Therefore, we define a threshold to truncate small singular values:

$$\hat{i} = \arg \min_i \left| \frac{\sum_{j=1}^i \sigma_j}{\sum \sigma} - r \right| \quad (12)$$

where \hat{i} is the index of truncation and r is the desired threshold ratio of the sum of singular values up to index j to the sum of all singular values [11].

It is important to note that as index increases, the amount of incorporated singular values of the matrix increase as well and that small perturbations in the observations can cause significant perturbations in the solution [28]. Problems to be aware of include choosing a truncation parameter large enough as to not lose a large part of the detected signals and small enough as to not incorporate too much noise.

TSVD is used for dimensionality reduction and produces Figure 13 on a given data set. This method is not sophisticated enough so we explore another process that uses a way to incorporate known properties of the solution into the solution method.

We impose restraints on the regularization term to develop a general regularized method with total variation to solve the nonlinear EIT using the Generalized Krylov Subspace iterative algorithm. The goal is to majorize the linearized EIT problem at each iteration and minimize the function through a quadratic tangent majorant [5]. This finds a surrogate function that locally approximates the objective function with difference minimized at a current point, upper bounding the objective function up to a constant. The product is a vector in which we need to re-weight and reshape to produce the approximation of the vector that characterizes the image seen in Figure 13

2.4 The EIT Deep Neural Network Model

EIT requires the implementation of feasible reconstruction methods capable of guaranteeing trustworthy image generation [18]. DNNs have a powerful ability to express complex nonlinear functions for which untrained voltage measurement samples are used as input for the trained DNN and an estimate for image reconstruction of the internal conductivity distribution is the output [30].

The nonlinear approach of DNNs allows them to efficiently simplify the EIT mathematical problem:

$$G = F(V; I) \quad (13)$$

where I is a vector storing the boundary current impulse measurements sent out and V is the resulting boundary voltage measurement [18]. The function maps these values

to the pixel value distribution with respect to varying conductivities, representing the backwards model of the forward problem:

$$V = U(\sigma; I)$$

in which the boundary voltage measurements V are calculated using the conductivity σ and current I measurements [18]. As the EIT problem is ill-posed, we solve for the inverse to reconstruct the conductivity measurements to more accurately represent their true values. This yields a more accurate pixel value distribution to be recovered.

Therefore, function (13) is then to be reconstructed using a DNN model. This eliminates the need to linearize the inverse problem. Additionally, DNNs can also overcome shortcomings of other proposed NN structures that may lead to overfitting of data, parameter dependence, or limited ability to express complex functions [13].

We begin by establishing the DNN architecture. DNNs predict a discrete class label and fit a continuum set of data points. When data training, we use boundary voltage data as the input layer and 3 hidden layers, each with 70 nodes. The output layer then reflects the distribution of conductivity within the object field, as can be modeled by Figure 5. The learning process is extracting previously unknown features of the solution layer by layer and mapping the detected features of original spatial data samples to a new continuum [13].

We simulate an object that places N , in our case $N = 16$, electrodes evenly around its exterior. Then, once electrical impulse signals are sent through the object, we record $N \times (N - 3)$ independent voltage measurements for each data set [34]. Thus, 208 voltage measurements are recorded. The goal of our DNN is to accurately predict the conductivity values that generate these measurements. We use electrical impedance maps (EIM) (Figure 6) as a visual representation of the conductivity distribution in each object [14].

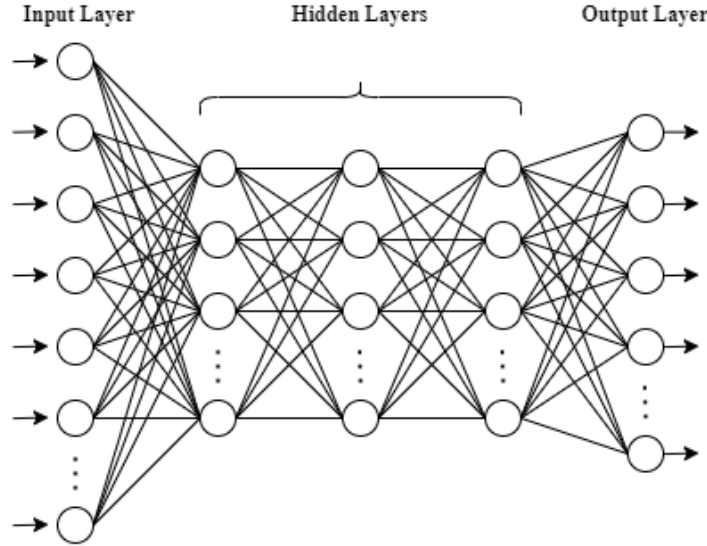


Figure 5: Deep Neural Network Structure

We start by generating data for the DNN to train on. We utilize EIDORS simulation software to solve the EIT forward problem when reconstructing the EIMs. Each data set generates an EIM with one circular anomaly, of varying size and position, within a boundary Figure 7. The voltage and conductivity values are recorded for the respective EIM using EIDORS. This process was repeated until 16,000 unique datasets are generated. Of these 16,000, 3,200 datasets are withheld from the neural network. Gaussian noise is added to the withheld datasets to mimic a realistic EIT process. These datasets are then used to test the accuracy of the trained DNN.

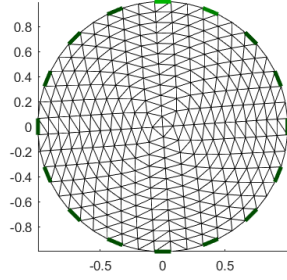


Figure 6: Empty Electrical Impedance Map.

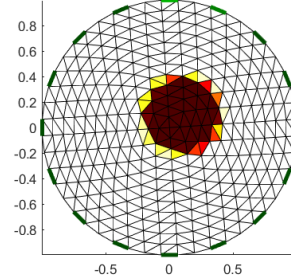


Figure 7: Sample formation of a single circular anomaly and the distribution of known conductivity we aim to assimilate with the DNN.

Before training the DNN, we implement batch normalization to prevent overfitting and to increase the efficiency of our model. The first hidden layer is trained after we input a known boundary voltage from an EIM. The output of the previous hidden layer is used as the input for the subsequent layer. This process is repeated for the remainder of each of the hidden layers. The relationship between the input, the voltage measurement that each electrode deploys, and the internal conductivity distribution is determined.

Our neural network model utilizes a rectified linear unit activation function for all three hidden layers. A dropout method is also implemented, in which weights within the hidden nodes are set to zero at random in order to prevent overfitting. The learning rate of the DNN is fixed at .0001, the number of training epochs is 400, and batch size is 10.

Untrained samples of voltage measurements are used as input and the reconstructed image of the internal conductivity distribution is used as the output for testing the accuracy of the trained DNN. Of the 3,200 generated data sets that are not used in the training process, approximately 8 are used for assessing the efficacy of the DNN.

3 Results

This section evaluates the impact of derivative operators on one-dimensional and two-dimensional systems, how the implementation of iterative and non-iterative methods compare, and the performance of the trained DNN with respect to producing accurate conductivity distribution maps.

3.1 Derivative Operator Implementation using Iteratively Reweighted Least Squares

We begin by examining how derivative operators (3), (6), (7), (8), and (9) perform at reconstructing a one dimensional image. Figures 8, 9, 10, 11, and 12 represent the respective plots of the true image in blue versus the estimated image in red using Tikhonov Regularization implemented with the respective derivative operator.

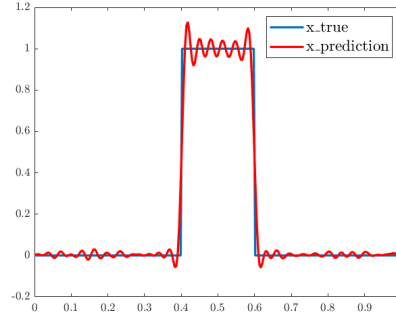


Figure 8: One-dimensional image reconstruction using the first order derivative approximation (3).

Figure 8 shows the effect of utilizing derivative operator (3) in the Tikhonov Regularization process, approximating the solution to equation (2). It can be seen that the minimization function predicts where the edges are positioned in the image. However, where the image displays horizontal lines, the minimization function produces minor derivations and some oscillating behavior.

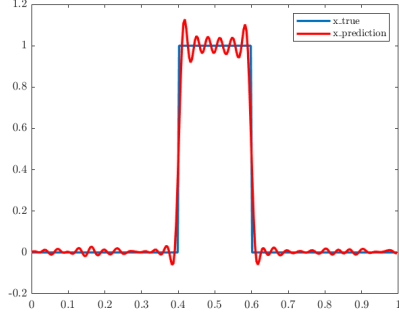


Figure 9: One-dimensional image reconstruction using the second order derivative approximation [6](#)

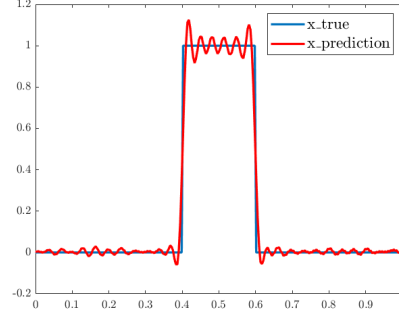


Figure 10: One-dimensional image reconstruction using the third order derivative approximation [8](#)

Figures [9](#) and [10](#) depict similar results as to Figure 8 using the same Tikhonov Regularization process. This tells us that while we would expect second and third order derivative operators to produce more accurate images, when operating in a one-dimensional system, such operators show singularities due to a limitation in the fundamental structure. Second and third order derivative operators improve performance in higher dimensional settings due to their nature of approximating gradients beyond what is computed using first derivative operators, hence why the figures look almost identical to that of Figure [8](#)

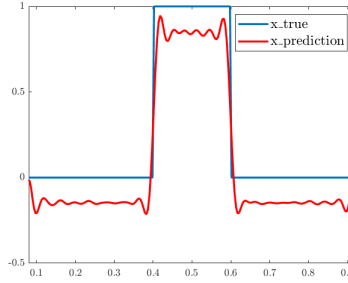


Figure 11: One-dimensional image reconstruction using the Laplacian operator [7](#).

Figure [11](#) is another image reconstruction, using derivative operator [8](#). As we are in a one-dimensional system, the Laplacian operator generates broad discrepancies between the objective and minimization function. We can see that the implementation of [8](#) in this example generates an image that does not approximate differentiable intervals precisely. Due to an imposed boundary condition, the edges are approximated more accurately. To depict the magnitude of perturbations at the right and left-hand edges of the plot, the horizontal and vertical scales of Figure [8](#) have been altered. We can observe small perturbations on the horizontal regions that are comparable to those of Figures [8](#), [9](#), and [10](#)

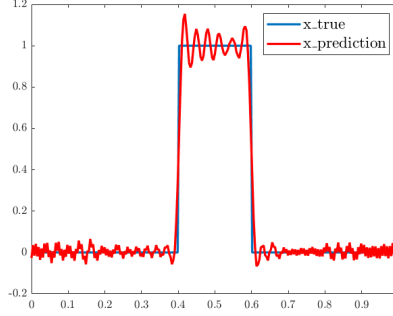


Figure 12: One-dimensional image reconstruction using the integral-based operator [9](#)

Figure [12](#) shows the effect of implementation of an integral operator [9](#) in Tikhonov Regularization for reconstructing a one-dimensional image. We can see that the integral operator leads to the approximation of an image with larger discrepancies than those of any of the other operators for this specific dataset. As with higher order derivative approximations, the integral operator performs more accurately when used in a higher dimensional environment. As image processing kernels of integral operators are normally smooth, the integral operators are compact in higher dimensional Banach spaces [21](#). Therefore, the solutions are not continuously dependent on the fed-in data. Hence small perturbations in the data lead to the large perturbations in the projected solution shown.

Table 1: Different Operators and their x error.

Operator	x error
First Derivative	0.129444433665467
Second Derivative	0.129207766790341
Third Derivative	0.129452952712647
Integral Operator	0.132211275817562
Laplacian	0.594913947842126

Table [1](#) shows the computed x_{error} caused by the inconsistencies between the true and approximated solutions that we observe in Figures [8](#), [9](#), [10](#), [11](#), and [12](#). This value was computed using the formula [3](#):

$$x_{error} = \frac{||x_{true} - x_{predicted}||_2^2}{||x_{true}||_2^2}$$

As we were comparing how accurately each derivative operator detected the edges in the one-dimensional image, we utilized data in which the true output was known. This way, we could use a method of measuring the magnitude of how closely each derivative operator got to approximating the directionality changes throughout. Therefore, x_{true} is the true solution value that characterizes information that is used in constructing the image, and $x_{predicted}$ is the Tikhonov Regularization's computed solution value. We can see that the implementation of [6](#) had the closest solution approximation by just over two ten-thousandths of a point.

3.2 Iterative and Non-Iterative Method Performances

Figure 13 and Figure 14 compare the performance accuracy of using the Truncated Singular Value Decomposition and the Generalized Krylov Method process to calculate vectorized information needed for reconstructing an image of a subject's region of interest respectively. It is seen that there is not a significant difference between the quality of the images, though the Generalized Krylov Method does show a slight improvement in sharpness and definition of the main anomaly as well as those surrounding it.

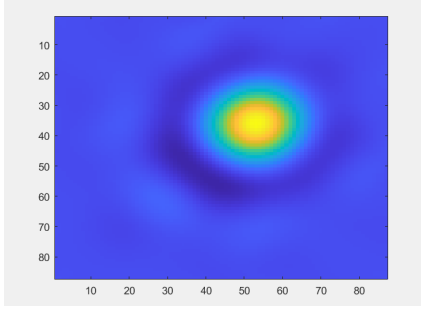


Figure 13: Product of using the truncated singular value decomposition non-iterative method.

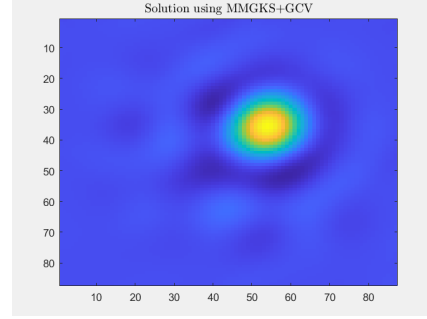


Figure 14: Product of using the Generalized Krylov Subspace iterative process.

3.3 Deep Neural Networks

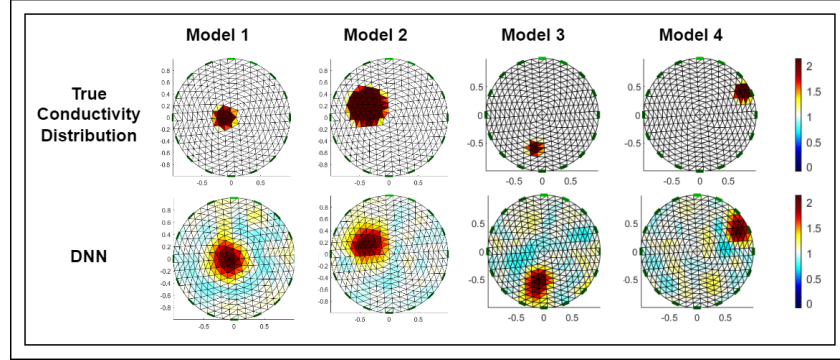


Figure 15: Models 1-4 and their reconstructions generated using a DNN.

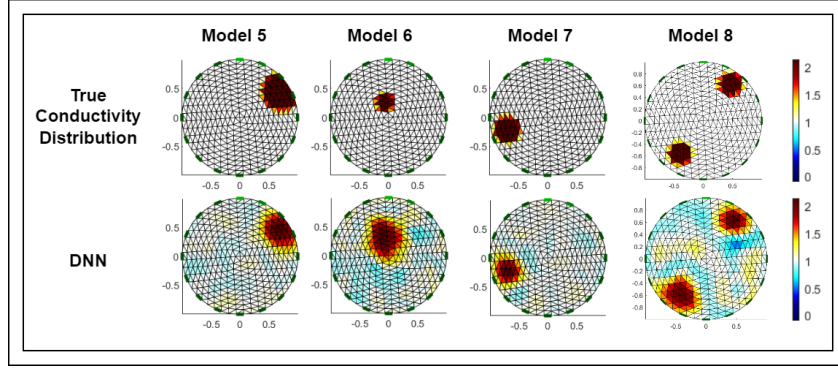


Figure 16: Models 5-8 and their reconstructions generated using a DNN. Model 8 includes two anomalies, whereas the DNN was trained solely on EIMs containing one anomaly.

Table 2: Reconstructed Models and their MSE.

Reconstructed Models	MSE
Model 1	0.0052
Model 2	0.0210
Model 3	0.0179
Model 4	0.0038
Model 5	0.0190
Model 6	0.0061
Model 7	0.0270
Model 8	0.0202

Table 2 shows the Mean Squared Error (MSE) for each model in Figure 15 and Figure 16. To calculate MSE, we utilized the equation

$$\text{MSE}(\sigma^*) = \frac{\|\sigma^* - \sigma\|_2^2}{N}$$

where σ^* is the true conductivity distribution, and σ is the prediction calculated by the DNN [18]. Then N is the number of observations, in our case 3,200.

4 Discussion

4.1 Conclusions

This study sought to evaluate the performance of different strategies for solving the EIT inverse problem. We proposed that through investigating both traditional approaches and a deep neural network structure, we would find an optimal solution method for reconstructing an accurate image. To test this, we compared traditional approaches such as the Generalized Krylov Method, the Truncated Singular Value Decomposition, and iteratively reweighted least squares to novel methods such as deep neural networks using MatLab and EIDORS software.

We began by deriving a baseline minimization function (2) to perform Tikhonov Regularization with to make more efficiently be able to analyze the results of implementing different definitions of the L derivative operator. Specifically, we compared operators that utilized approximations of the first, second, and third derivatives, as well as the integral and Laplacian operators. The reconstructions generated in Figures 8, 9, 10, 11 and 12 showed that the derivative approximations produced a more accurate depiction of the one-dimensional signal when compared to the integral and Laplacian operators. Since the Laplacian and integral operators are primarily used in higher dimensional systems, they struggled to approximate the signal on both differentiable and non-differentiable intervals, generating error due to the discontinuous nature of the signal [21, 37]. As derivative operators are able to detect rapid changes in intensity, the first, second, and third derivative approximations were able to detect the sharp edges of the one-dimensional signal. However, higher derivative approximations are more sensitive to noise than lower derivative approximations. Thus, while the second derivative approximation was able to detect the edges more accurately than the first derivative approximation, it was also able to resist noise to a higher degree compared to the third derivative approximation.

To study traditional methods on a larger scale, for the purpose of EIT, we utilized simulated data to construct a more realistic sensitivity matrix as our A in the standard matrix-vector equation. In combination with the first derivative operator, we reconstructed a conductivity distribution map (Figure 13), first using the Truncated Singular Value Decomposition approach, and compared the result to the map produced using a Generalized Krylov Subspace algorithmic framework (Figure 14). Although the TSVD is effective in reducing the dimensionality of the large system, spatial resolution is compromised due to its non-iterative nature. Therefore, the image we were able to produce lacked clarity in depicting the anomalies surrounding the primary anomaly. The Generalized Krylov process proved to be more effective in detecting small changes in conductivity about the subject's region of interest. As the Generalized Krylov method is an iterative process that updates a solution estimation until an error threshold is reached, the image in Figure 14 represents the ability for iterative processes to closely approximate a solution. Therefore, the Generalized Krylov iterative processes work well in not only breaking the large system down into smaller parts for reduced computational cost, but they also improve the spatial resolution of reconstructed images.

This study also explored the implementation of a deep neural network as a novel method to aid in EIT reconstruction. The deep neural network was then used for product comparison using the results obtained through methods discussed in 2.1, 2.2 and 2.3. We constructed a deep neural network using processes described in 2.4. Following the training of the neural network, the DNN was then tested on withheld data. Eight models were

produced from the 3,200 withheld datasets, each generating an EIM that was compared to the true conductivity distribution image. Additionally, the Mean Squared Error (MSE) between the true and constructed maps was calculated. We concluded that the neural network excelled in reconstructing the simulated images consisting of one central anomaly, although smaller anomalies on the boundary of the EIM proved challenging to detect. As small anomalies have reduced effect on the overall voltage distribution, the neural network had trouble discerning their positions. This reduced effect also caused similar voltage measurements to be recorded, resulting in the duplication of the same EIM for multiple datasets. This made our neural network susceptible to overfitting as the predicted EIM often bore no resemblance to the actual image. To correct this fault, we implemented a dropout method in which the weight of nodes in the hidden layer was reduced to zero at random. This prevented the neural network from becoming dependent on any particular node, thus limiting the model’s ability to overfit data [18]. We then decided to test our DNN’s ability to detect multiple anomalies. In Model 8 of Figure 16, our DNN is tested on an image with two circular anomalies. Our DNN was able to reconstruct this image, despite it solely being trained on datasets in which one anomaly was present. The MSE for the reconstructed models are given in Table 2 and suggest that our modified neural network is able to use voltage measurements to accurately predict conductivity distributions.

4.2 Limitations and Future Work

Future work would include constructing a sensitivity matrix using the information output in the conductivity and voltage distribution maps. As we utilized a circular triangulated space to test our deep neural network on, we would need to understand how to convert the circular domain into a grid in a rectangular domain, since the traditional methods we investigated were dependent on a cartesian set of data. This would allow us to then compare the spatial resolution in images constructed using traditional methods to that of images constructed using the deep neural network, as we would then be analyzing results drawn from the same dataset. Additionally, we found that various models proposed alternative means of calculating error. As a result, there was not a quantitative approach to compare the neural network to the traditional methods. In order to progress on the EIT inverse problem, a uniform strategy of accuracy comparison must be implemented. Additionally, we would be interested in investigating the implications of a semi-array electrode framework as opposed to the full ring electrode framework simulated in our study. This would broaden the spectrum of applications of EIT as it would eliminate the need to place electrodes around the entire perimeter of the region of interest within a subject.

Acknowledgements

We would like to thank Dr. Fabio Milner, Director of the Simon A. Levin Mathematical, Computational and Modeling Sciences Center (Levin Center), for giving us the opportunity to participate in the Quantitative Research in the Life and Social Sciences program. We would also like to thank Co-Directors Dr. Abba Gumel and Dr. John Nagy for their efforts in planning and executing the program's instruction and activities. We also recognize the work of the many administrative staff and tutors who supported this effort. This research was conducted as part of 2022 QRLSSP at the Levin Center (MCMSC) at Arizona State University (ASU). This project has been partially supported by grants from the National Science Foundation (NSF Grant-DMS-1757968 and NSF Grant FAIN-2150492), the National Security Agency (NSA Grant H98230-20-1-0164), the Office of the President of ASU, and the Office of the Provost of ASU.

References

- [1] Andy Adler, John H Arnold, Richard Bayford, Andrea Borsic, Brian Brown, Paul Dixon, Theo JC Faes, Inéz Frerichs, Hervé Gagnon, Yvo Gärber, et al. Greit: a unified approach to 2d linear eit reconstruction of lung images. *Physiological measurement*, 30(6):S35, 2009.
- [2] Holder Adler. *Electrical Impedance Tomography*. 2021.
- [3] Babak Maboudi Afkham, Julianne Chung, and Matthias Chung. Learning regularization parameters of inverse problems via deep neural networks. *Inverse Problems*, 37(10):105017, 2021.
- [4] Abdulbasit Alazzawi. Edge detection-application of (first and second) order derivative in image processing: Communication. *Diyala Journal of Engineering Sciences*, 8(4):430–440, 2015.
- [5] Eman Alruwaili and Jing Li. Majorization–minimization total variation solution methods for electrical impedance tomography. *Mathematics*, 10(9):1469, 2022.
- [6] John C Bancroft. Differential operators 1: the first derivative. *CREWES Report*, 2008.
- [7] Bebis. Spatial filtering. 2013.
- [8] VICTOR CHURCHILL. Iteratively reweighted regularization methods for image reconstruction from non-uniform fourier data. 2018.
- [9] Jérémie Dardé, N Hyvonen, A Seppanen, and Stratos Staboulis. Simultaneous reconstruction of outer boundary shape and admittivity distribution in electrical impedance tomography. *SIAM Journal on Imaging Sciences*, 6(1):176–198, 2013.
- [10] Digital Image Processing. Laplacian operator, np.
- [11] Shuyong Duan, Botao Yang, Fang Wang, and Guirong Liu. Determination of singular value truncation threshold for regularization in ill-posed problems. *Inverse Problems in Science and Engineering*, 29(8):1127–1157, 2021.
- [12] Silvia Gazzola, Sebastian James Scott, and Alastair Spence. Flexible krylov methods for edge enhancement in imaging. *Journal of Imaging*, 7(10):216, 2021.
- [13] Sarah Jane Hamilton and Andreas Hauptmann. Deep d-bar: Real-time electrical impedance tomography imaging with deep neural networks. *IEEE transactions on medical imaging*, 37(10):2367–2377, 2018.
- [14] Delin Hu, Keming Lu, and Yunjie Yang. Image reconstruction for electrical impedance tomography based on spatial invariant feature maps and convolutional neural network. In *2019 IEEE International Conference on Imaging Systems and Techniques (IST)*, pages 1–6. IEEE, 2019.
- [15] Behzad Kamgar-Parsi and Azriel Rosenfeld. Optimally isotropic laplacian operator. *IEEE Transactions on Image Processing*, 8(10):1467–1472, 1999.

- [16] Yongchae Kim and Hiroyuki Kudo. Nonlocal total variation using the first and second order derivatives and its application to ct image reconstruction. *Sensors*, 20(12):3494, 2020.
- [17] Ville Kolehmainen, Matti Lassas, and Petri Ola. Electrical impedance tomography problem with inaccurately known boundary and contact impedances. *IEEE transactions on medical imaging*, 27(10):1404–1414, 2008.
- [18] Xiuyan Li, Yong Zhou, Jianming Wang, Qi Wang, Yang Lu, Xiaojie Duan, Yukuan Sun, Jingwan Zhang, and Zongyu Liu. A novel deep neural network method for electrical impedance tomography. *Transactions of the Institute of Measurement and Control*, 41(14):4035–4049, 2019.
- [19] Habte Tadesse Likassa and Wen-Hsien Fang. Robust regression for image alignment via subspace recovery techniques. In *Proceedings of the 2018 VII International Conference on Network, Communication and Computing*, pages 288–293, 2018.
- [20] Rui Liu, Lu He, Yan Luo, and Hengyong Yu. Singular value decomposition-based 2d image reconstruction for computed tomography. *Journal of X-ray Science and Technology*, 25(1):113–134, 2017.
- [21] Yao Lu, Lixin Shen, and Yuesheng Xu. Integral equation models for image restoration: high accuracy methods and fast algorithms. *Inverse Problems*, 26(4):045006, 2010.
- [22] Michael Lukashewitsch, Peter Maass, and Michael Pidcock. Tikhonov regularization for electrical impedance tomography on unbounded domains. *Inverse Problems*, 19(3):585, 2003.
- [23] Georgios Lymeropoulos, Panagiotis Lymeropoulos, Victoria Alikari, Chrisoula Dafogianni, Sofia Zyga, and Nikoletta Margari. Applications for electrical impedance tomography (eit) and electrical properties of the human body. In *GeNeDis 2016*, pages 109–117. Springer, 2017.
- [24] MIT. *Chapter 4*. Number 42. MIT.
- [25] JP Morucci, M Granie, M Lei, M Chabert, and WW Dai. Direct sensitivity matrix approach for fast 3-d reconstruction in electrical impedance imaging. In *Proceedings of 16th Annual International Conference of the IEEE Engineering in Medicine and Biology Society*, volume 1, pages 538–539. IEEE, 1994.
- [26] Meghdoot Mozumder, Tanja Tarvainen, Jari P Kaipio, Simon R Arridge, and Ville Kolehmainen. Compensation of modeling errors due to unknown domain boundary in diffuse optical tomography. *JOSA A*, 31(8):1847–1855, 2014.
- [27] Jennifer L Mueller and Samuli Siltanen. *Linear and nonlinear inverse problems with practical applications*. SIAM, 2012.
- [28] Sungho Oh, Te Tang, AS Tucker, and RJ Sadleir. Normalization of a spatially variant image reconstruction problem in electrical impedance tomography using system blurring properties. *Physiological measurement*, 30(3):275, 2009.

- [29] Dianne P O’Leary. Robust regression computation using iteratively reweighted least squares. *SIAM Journal on Matrix Analysis and Applications*, 11(3):466–480, 1990.
- [30] Cameron Dennis Pain, Gary F Egan, and Zhaolin Chen. Deep learning-based image reconstruction and post-processing methods in positron emission tomography for low-dose imaging and resolution enhancement. *European Journal of Nuclear Medicine and Molecular Imaging*, pages 1–21, 2022.
- [31] Lothar Reichel and Qiang Ye. Simple square smoothing regularization operators. *Electronic Transactions on Numerical Analysis*, 33:63, 2009.
- [32] Paul Rodr guez and Brendt Wohlberg. Performance comparison of iterative reweighting methods for total variation regularization. In *2014 IEEE International Conference on Image Processing (ICIP)*, pages 1758–1762. IEEE, 2014.
- [33] Paul Rodriguez and Brendt Wohlberg. An iteratively reweighted norm algorithm for total variation regularization. In *2006 Fortieth Asilomar Conference on Signals, Systems and Computers*, pages 892–896. IEEE, 2006.
- [34] RJ Sadleir, SU Zhang, AS Tucker, and Sungho Oh. Imaging and quantification of anomaly volume using an eight-electrode ‘hemiarrray’eit reconstruction method. *Physiological measurement*, 29(8):913, 2008.
- [35] Fadil Santosa and Michael Vogelius. A backprojection algorithm for electrical impedance imaging. *SIAM Journal on Applied Mathematics*, 50(1):216–243, 1990.
- [36] Marko Vauhkonen, D nes Vad sz, Pasi A Karjalainen, Erkki Somersalo, and Jari P Kaipio. Tikhonov regularization and prior information in electrical impedance tomography. *IEEE transactions on medical imaging*, 17(2):285–293, 1998.
- [37] Xin Wang. Laplacian operator-based edge detectors. *IEEE transactions on pattern analysis and machine intelligence*, 29(5):886–890, 2007.
- [38] Brendt Wohlberg and Paul Rodriguez. An iteratively reweighted norm algorithm for minimization of total variation functionals. *IEEE Signal Processing Letters*, 14(12):948–951, 2007.
- [39] Peimin Yan, Shuozhong Wang, and Luming Shi. Electrical impedance tomography based on sensitivity theorem with singular value decomposition. In *2005 IEEE Engineering in Medicine and Biology 27th Annual Conference*, pages 1488–1491. IEEE, 2006.
- [40] Gengsheng L Zeng and Edward V DiBella. Non-iterative image reconstruction from sparse magnetic resonance imaging radial data without priors. *Visual Computing for Industry, Biomedicine, and Art*, 3(1):1–8, 2020.
- [41] Hongyu Zhou, Ting Kou, and Xu Song. Application of two-dimensional truncated singular value decomposition in image restoration. In *Journal of Physics: Conference Series*, volume 1976, page 012009. IOP Publishing, 2021.
- [42] Egon Zimmermann, Johan Alexander Huisman, Stefan van Waasen, and Walter Glaas. Fast eit data acquisition for geophysical applications. In *7th World Congress on Industrial Process Tomography*, number FZJ-2013-05372. Zentralinstitut f r Elektronik, 2013.